Ionospheric Analysis With Martian Mutual Radio Occultation

Parrott, Jacob; Svedhem, Håkan; Sánchez-Cano, Beatriz; Witasse, Olivier; Wilson, Colin; Müller-Wodarg, Ingo

DOI
10.1029/2024JE008854

Publication date
2025

Document Version
Final published version

Published in
Journal of Geophysical Research: Planets

Citation (APA)
Parrott, J., Svedhem, H., Sánchez-Cano, B., Witasse, O., Wilson, C., & Müller-Wodarg, I. (2025). Ionospheric Analysis With Martian Mutual Radio Occultation. *Journal of Geophysical Research: Planets*, *130*(6), Article e2024JE008854. https://doi.org/10.1029/2024JE008854

JGR Planets

RESEARCH ARTICLE
10.1029/2024JE008854

Ionospheric Analysis With Martian Mutual Radio Occultation

Jacob Parrott[1], Håkan Svedhem[2], Beatriz Sánchez-Cano[3], Olivier Witasse[4], Colin Wilson[4], and Ingo Müller-Wodarg[1]

[1]Imperial College London, London, UK, [2]TU Delft, Delft, The Netherlands, [3]School of Physics and Astronomy, University of Leicester, Leicester, UK, [4]European Space Research and Technology Centre, ESA-ESTEC, Noordwijk, The Netherlands

Key Points:

- Many low-SZA ionospheric profiles have been gathered
- All data sets for MEX-TGO Mutual Radio Occultation have now been made available to the community
- Temperature trends around 120 km do not follow the expected Solar Zenith Angles trend with direct solar heating

Correspondence to:
J. Parrott,
jdparrottuk@gmail.com

Citation:
Parrott, J., Svedhem, H., Sánchez-Cano, B., Witasse, O., Wilson, C., & Müller-Wodarg, I. (2025). Ionospheric analysis with Martian mutual radio occultation. *Journal of Geophysical Research: Planets*, *130*, e2024JE008854. https://doi.org/10.1029/2024JE008854

Received 21 NOV 2024
Accepted 18 MAY 2025

Author Contributions:
Conceptualization: Jacob Parrott
Data curation: Jacob Parrott
Formal analysis: Jacob Parrott, Beatriz Sánchez-Cano, Olivier Witasse, Ingo Müller-Wodarg
Funding acquisition: Ingo Müller-Wodarg
Investigation: Jacob Parrott
Methodology: Jacob Parrott, Håkan Svedhem, Beatriz Sánchez-Cano, Ingo Müller-Wodarg
Project administration: Ingo Müller-Wodarg
Resources: Ingo Müller-Wodarg
Software: Jacob Parrott
Supervision: Håkan Svedhem, Ingo Müller-Wodarg
Validation: Jacob Parrott, Håkan Svedhem, Beatriz Sánchez-Cano, Ingo Müller-Wodarg
Visualization: Jacob Parrott
Writing – original draft: Jacob Parrott
Writing – review & editing: Jacob Parrott, Håkan Svedhem, Beatriz Sánchez-Cano, Olivier Witasse, Colin Wilson, Ingo Müller-Wodarg

Abstract This study presents a comprehensive analysis of the Martian ionosphere using Mutual Radio Occultation (RO) observations between Mars Express and Trace Gas Orbiter, featuring 71 full vertical profiles out of a total of 124 measurements. Among these, 35 measurements were taken from regions with Solar Zenith Angles lower than 40°. The profiles also represent the largest data set for the lower M1 ionospheric layer during the midday ever measured. This paper has also been submitted with a comprehensive data set, which marks the first time MEX-TGO RO data has been made available to the community. Additionally, neutral temperature profiles have been extracted from the measurements. We find unexpected features in the lower thermosphere temperature behavior which we conclude is likely due to the effects of local circulation and associated dynamical heating rather than solar-controlled.

Plain Language Summary This article shows the results of 71 Martian mutual radio occultation (RO) measurements. This new measurement technique is similar to conventional RO, where a radio signal is sent from a satellite orbiting another planet to a ground station on earth. As this signal passes through the planetary atmosphere, it bends slightly due to refraction and we can look at this amount of bending to infer things such as temperature and electron density. Mutual RO (sometimes called crosslink or inter-satellite RO) is when we do not send the signal back to Earth, but we send the radio signal between two satellites orbiting the same planet. Mutual RO has a large advantage over conventional spacecraft-to-Earth RO because we can measure local times close to midday. This article uses these data sets from this new measuring technique to explore the trends of the ionosphere with varying amounts of irradiance from the sun. This article also uses ionospheric readings to predict the temperature around 120 km altitude and then finds that it is more controlled by dynamics (the transport of the air, like winds) instead of the direct heating from the sun.

1. Introduction

A radio occultation (RO) observation occurs when a radio transmitter and receiver are obscured from each other by a planetary atmosphere. Just before the signal is lost, the line of sight between the two antennas grazes the planet's limb, progressively penetrating deeper into the atmosphere until reaching a medium of sufficient opacity; be that a planetary surface for terrestrial planets, or a dense atmosphere on the gas giants. During this process, the signal traverses different atmospheric layers, each possessing varying refractive properties, resulting in a slight frequency shift. After accounting for the Doppler shift caused by the relative motion of the two spacecraft, this frequency shift can be analyzed to determine the refractive properties of the atmosphere. These properties can then be used to estimate the neutral atmosphere's density and the electron density of the ionosphere (e.g., Fjeldbo et al., 1971; A. Kliore et al., 2004; Withers, 2020). Traditionally, RO observations for planets other than Earth involve a spacecraft orbiting the planet and a ground station on Earth. However, this technique can also be performed between two spacecraft orbiting the same planet, a method known as mutual RO or Crosslink Occultation (Ao et al., 2015).

Since 1 November 2020, mutual RO observations have been conducted at Mars between ESA's Mars Express (MEX) and the ExoMars Trace Gas Orbiter (TGO) spacecraft, offering significant advancements in the study of the Martian atmosphere. A key advantage of mutual RO is its ability to provide a substantially broader spatial distribution of measurement coordinates and a wider range of Solar Zenith Angles (SZA). SZA is the value from the surface normal to direction of sun, so a SZA of 0° is at midday, directly under the sun, whereas 90° is at the sunset/sunrise terminator as seen from the surface of the planet. This expanded coverage is crucial for understanding atmospheric conditions across different regions of Mars. For instance, the primary factor influencing

Martian ionospheric densities is the SZA, with the Radio Occultation Science Experiment (ROSE) on the Mars Atmosphere and Volatile EvolutioN mission (MAVEN) achieving their lowest SZA measurement at 45° (Withers et al., 2024). Such angles are exceedingly rare, with our SPICE simulations indicating that only 0.1% occur below 70°, resulting in a lack of critical data for midday martian conditions. While lower SZA RO measurements can be found in the Mariner 9 (A. J. Kliore et al., 1972) and Viking 1 (Fjeldbo et al., 1977) archives, these only extend down to 47° and 53°, respectively (Vogt et al., 2016).

Although other instruments, such as mass spectroscopy and radar sounders, have explored regions near noon, RO provides a unique advantage by offering a complete cross-section of the atmosphere. This capability is particularly important for studying features like the M1 layer of the ionosphere (around 90–110 km), which remains largely unexplored in low SZA regions.

The first RO experiment beyond Earth was conducted at Mars by Mariner IV in 1965, which established a surface pressure of 5–9 mb (Kliore, 1974). The Martian ionosphere was first observed by the Mariner 9 spacecraft, which collected 114 profiles (Vogt et al., 2016; Withers et al., 2015) Further exploration of the ionosphere via RO was carried out in 1976 by the Viking orbiters (Hanson et al., 1977), which identified the subsolar peak electron density at an altitude of 120 km with a scale height of 10 km (Hantsch & Bauer, 1990). Over the following three decades, RO was employed to investigate the martian ionosphere using Mars Global Surveyor (MGS), Mars Express, and MAVEN (Hinson et al., 1999, Pätzold et al., 2004; Withers et al., 2020, respectively). This technique was also demonstrated by the Mars Cube One (MarCO-A) CubeSat in 2018 (Oudrhiri et al., 2020); however, due to pointing errors and the absence of an Ultra-Stable Oscillator, the ionosphere was not detected, particularly as the probe was focused on the nightside of Mars. The feasibility of conducting RO between two spacecraft at the same planet has also been explored, with an engineering demonstration of mutual RO performed between Mars Reconnaissance Orbiter and Mars Odyssey in 2007, resulting in three quality ionospheric soundings (Ao et al., 2015).

A more systematic exploration of MEX-TGO mutual RO has been conducted by Parrott et al. (2024), including the planning of occultation opportunities, the processing chain, initial results, and engineering recommendations for future missions. The extensive data sets, ranging from Level-1 to 4, generated by these measurements have been made available through the European Space Agency's Planetary Service Archive (Parrott, 2024).

This paper will elucidate the scientific implications of these measurements, focusing specifically on the sources of variability observed in the M2 (120–150 km) and M1 (90–110 km) peak densities and altitudes, as well as the inferred thermospheric temperatures. Through this analysis, we aim to enhance our understanding of the Martian atmosphere and its dynamic processes.

2. The Martian Ionosphere

The martian atmosphere, akin to other planetary atmospheres within the solar system, exhibits a radial structure characterized by a decrease in neutral density from the surface up to the interplanetary medium. The embedded ionosphere, located within the mesosphere and thermosphere, results from a balance of processes such as photoionization (and its secondaries) and recombination (Schunk & Nagy, 2009). The density of the dayside martian ionosphere is notably influenced by photoionization from sunlight, and impact ionization caused by photoelectrons and their secondaries. On the nightside, some ionization persists due to electron precipitation (Fox et al., 1993).

The structure of the martian ionosphere is primarily governed by photochemical processes as photochemical timescales are smaller than transport timescales (Fox et al., 2017; Matta et al., 2013). Consequently, the ionospheric layers generally conform to an alpha-Chapman profile. This profile arises from the interaction between the exponential increase in neutral density with decreasing altitude and the optical depth of radiation at specific wavelengths, as described in the equation for the two superimposed ionospheric layers.

$$N_e(z,\chi) = \sum_{l=M2}^{M1} \exp\left\{\left[\frac{1}{2}\left(1 - \frac{z - z_l}{H_l} - \exp\left(-\frac{z - z_l}{H_l}\right)\sec\chi\right)\right]\right\} \quad (1)$$

The topside of the Chapman profile reflects the e-folding nature of neutral atmospheres, while the bottom side is shaped by reduced radiation penetration at lower altitudes. The Martian ionosphere typically consists of two such

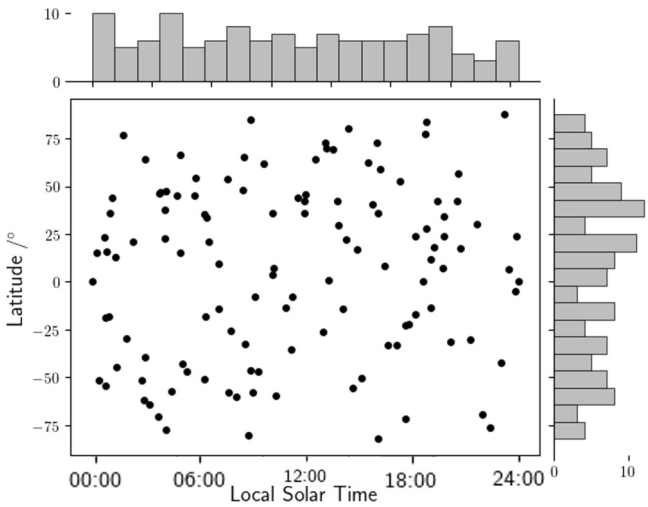

Figure 1. Distribution of 124 mutual radio occultations with latitude on the *y*-axis and local solar time on the *x*-axis. Histograms placed on the axis to show the even spread, with 19 bins for the ±90° latitude *y*-axis (9.5° per bin) and 19 bins for the 24 hr local time *x*-axis (75 min per bin).

layers: the primary M2 layer, located at approximately 120–150 km, and the secondary M1 layer, found at around 90–110 km. The M2 layer primarily forms due to the photoionization of CO_2 by extreme ultraviolet (EUV) radiation, peaking where the optical depth for this wavelength reaches unity. Below this altitude, the M1 layer's height is determined by the penetration depth of soft X-rays, where its formation is largely driven by photoionization and then secondary ionizations from photoelectrons generated by these higher-energy soft X-ray photons (Fox, 2004; Martinis et al., 2003). Research has shown that internal factors like Mars's crustal magnetic field can also significantly influence the Martian ionosphere (Andrews et al., 2023; Langlais et al., 2019; Lillis et al., 2008; Majeed et al., 2025; Matta et al., 2015). Finally, there are also known effects of dust storms where the dust loading increases infra-red absorption and heats the lower atmosphere. This causes the atmosphere to thermally expand, leading to an increase in peak density altitudes (Felici et al., 2020; Girazian et al., 2020; Peter et al., 2023).

Due to conventional RO only exploring regions near the terminator, there has been considerable work on the difference between the dawn and dusk ionospheric dynamics. Segale et al. (2024) used MAVEN ROSE data to show that dawn regions have a significantly higher M2 altitude and density during perihelion, as opposed to dusk, which varies less with solar distance. Whilst investigating the systematic difference between MAVEN ROSE and LPW measurements, Felici et al. (2022) postulated that the dawn ionosphere exhibits higher variability in general than the dusk regions. Pilinski et al. (2019) suggested this dawn/dusk asymmetry is due to diurnal variations in coupling between the ionosphere and the neutral atmosphere. The neutral atmosphere (between 150 and 300 km) is known to be at its highest density and temperatures at dusk, instead of the middle of the day (Gupta et al., 2019). This would infer a higher molecular collisionallity at dusk, therefore effecting the coupling in the ionosphere-thermosphere system.

Although not the primary focus of this work, the nightside ionosphere is also of interest, where it has an irregular morphology and is sustained by electron impact ionization (Girazian et al., 2017a, 2017b). Observations have revealed density structures in the ionosphere, with electron densities peaking at around 5×10^3 cm^{-3} on the nightside (Withers et al., 2022). Additionally, the ionosphere exhibits irregularities similar to those found in Earth's equatorial E region, particularly in areas where the magnetic field is parallel to the surface (Tian et al., 2022).

3. The Data

At the time of writing, the MEX-TGO mutual RO campaign is still ongoing, with a cadence of roughly two per week. So far, we have conducted 124 measurements across the full range of latitudes and local times, as illustrated in Figure 1. Of these, 71 successfully yielded day-side vertical electron density profiles. The measurements span SZA values from as low as 5.2° close to the sub-solar point to 171° near the anti-solar point. Notably, 35 of these observations were conducted below the minimum SZA of 46.8° typically achievable by the ROSE MAVEN experiment, highlighting our ability to comprehensively study for the first time the near-noon dayside ionosphere. Additionally, 18 readings were obtained from the nightside; however, only the day-side vertical profiles and their corresponding specifications are presented in this article. Numerous other mutual RO measurements have been discarded due to reasons listed in Parrott et al. (2024). In brief, these reasons include synchronization errors between MEX and TGO, large spectral artifacts due to Electra antenna faults and MELACOM broadcasting a HAIL sequence which included regular silent periods (making carrier tone extraction impossible). The main purpose of these profiles is to study the photochemical region of the ionosphere (less than 200 km). The electron densities in the diffusion region higher up are considered too low to be considered reliable with the current noise floor of the RO measurements. These specifications are detailed in Table 1, and the corresponding profiles are displayed in Figures 2 and 3. One may notice the occasional profile having missing values (e.g., the 01/02/23 profile in panel I of Figure 2), this is due to omission of portions of signal due to of spectral artifacts in the readings from the receiving antenna (called Electra).

Table 1
Specification Table for All Mutual Radio Occultation Measurements

Date	UTC start	UTC of occultation	SZA (°)	Lat (°N)	Lon (°E)	Local time	Max altitude (km)	Scheme	Solar distance (AU)	$F_{10.7}$	Ly-a (mWm^{-2})
02/04/21	15:09:00	15:18:16	14	13	144	11:04	399	Ingress	1.62	71	1.44
06/04/21	03:30:00	03:38:49	34	43	352	11:01	415	Ingress	1.62	71	1.45
14/04/21	23:32:00	23:33:09	82	43	61	05:55	394	Egress	1.63	75	1.47
18/05/21	07:07:00	07:08:32	63	80	346	11:18	368	Egress	1.65	79	1.49
25/05/21	00:08:00	00:09:05	36	54	153	11:07	321	Egress	1.65	79	1.45
22/07/21	00:06:00	00:07:20	32	−8	6	12:18	374	Egress	1.67	91	1.49
06/04/22	02:14:21	02:23:47	62	4	224	07:55	387	Ingress	1.42	117	1.72
27/04/22	13:52:20	13:52:55	50	−17	13	15:28	326	Egress	1.42	117	1.66
18/05/22	05:00:27	05:09:23	39	−56	276	10:52	343	Ingress	1.42	117	1.64
27/05/22	13:21:22	13:22:00	41	18	246	10:59	407	Egress	1.39	121	1.79
01/06/22	11:01:00	11:09:50	69	−35	263	06:46	347	Ingress	1.39	121	1.74
13/06/22	03:18:23	03:28:08	73	−14	288	17:07	350	Ingress	1.39	121	1.73
30/06/22	14:06:29	14:15:16	39	−47	261	14:41	379	Ingress	1.38	99	1.75
08/07/22	10:46:11	10:55:28	32	−47	17	13:57	379	Ingress	1.38	135	1.75
19/07/22	19:49:30	19:58:45	5	−30	322	11:56	380	Ingress	1.39	146	1.82
25/08/22	09:02:31	09:03:14	59	21	164	14:37	397	Egress	1.41	118	1.67
30/08/22	14:49:09	14:49:57	51	23	112	13:30	391	Egress	1.41	120	1.72
17/09/22	04:50:41	04:51:41	59	−59	346	07:44	371	Egress	1.43	137	1.72
19/09/22	06:00:57	06:01:21	58	−54	350	07:49	379	Egress	1.43	136	1.69
28/09/22	14:05:55	14:06:52	66	−46	307	07:03	373	Egress	1.44	136	1.71
13/10/22	15:14:55	15:14:54	70	−51	227	17:08	334	Egress	1.44	136	1.69
22/10/22	01:41:59	01:42:40	69	−52	149	16:57	378	Egress	1.47	103	1.67
27/10/22	20:43:17	20:52:23	68	47	240	14:28	425	Ingress	1.48	126	1.76
31/10/22	09:34:47	09:35:14	21	−33	46	11:58	367	Egress	1.49	129	1.79
11/11/22	04:36:05	04:36:43	67	29	168	08:11	399	Egress	1.50	135	1.73
24/11/22	07:47:32	07:56:41	75	−82	289	11:12	379	Ingress	1.52	104	1.85
07/12/22	14:38:51	14:39:33	80	24	45	17:09	403	Egress	1.53	142	1.81
14/12/22	06:03:10	06:04:38	77	65	209	15:17	409	Egress	1.54	157	1.74
19/12/22	19:33:50	19:34:17	53	42	45	14:15	418	Egress	1.55	152	1.73
21/12/22	22:19:24	22:28:18	41	−40	4	13:05	380	Ingress	1.55	136	1.75
22/12/22	16:28:43	16:29:09	60	59	97	12:49	377	Egress	1.55	131	1.78
27/12/22	04:07:52	04:16:36	33	−33	312	12:07	380	Ingress	1.56	152	1.86
04/01/23	08:44:08	08:53:03	27	−8	294	10:18	353	Ingress	1.57	150	1.85
09/01/23	05:10:05	05:18:19	80	48	138	17:14	369	Ingress	1.57	182	1.75
27/01/23	01:14:13	01:23:28	74	12	214	07:02	384	Ingress	1.59	140	1.79
01/02/23	03:27:34	03:37:18	81	83	227	06:52	397	Ingress	1.60	131	1.86
09/02/23	00:07:25	00:16:29	76	77	5	07:42	407	Ingress	1.61	203	1.87
15/02/23	17:21:54	17:31:12	63	73	231	11:44	391	Ingress	1.61	171	1.81
23/02/23	14:03:27	14:12:27	54	64	339	10:40	368	Ingress	1.62	147	1.87
26/02/23	18:39:46	18:48:46	59	62	275	08:58	365	Ingress	1.62	156	1.87
10/03/23	03:53:34	04:02:40	32	45	299	12:31	359	Ingress	1.63	170	2.01
20/03/23	15:17:13	15:26:23	54	69	212	11:26	434	Ingress	1.64	157	1.96
17/04/23	14:21:09	14:22:09	77	−58	151	12:33	381	Egress	1.66	175	1.88

Table 1
Continued

Date	UTC start	UTC of occultation	SZA (°)	Lat (°N)	Lon (°E)	Local time	Max altitude (km)	Scheme	Solar distance (AU)	$F_{10.7}$	Ly-a (mWm^{-2})
01/05/23	20:57:44	21:06:43	26	28	206	13:50	410	Ingress	1.66	156	2.05
08/05/23	06:20:01	06:29:18	29	42	123	13:37	416	Ingress	1.66	164	1.94
15/05/23	05:34:23	05:43:25	53	62	230	15:32	429	Ingress	1.66	139	1.86
27/06/23	23:05:49	23:05:49	13	36	326	11:23	389	Egress	1.66	158	1.98
20/07/23	15:21:38	15:21:32	48	57	259	08:39	404	Egress	1.65	188	1.90
24/07/23	23:20:47	23:20:41	63	88	246	12:59	328	Egress	1.65	188	1.92
19/08/23	20:15:50	20:16:14	83	54	278	19:29	433	Egress	1.63	156	2.03
24/08/23	05:52:15	05:52:51	37	−13	64	12:01	325	Egress	1.63	156	1.86
28/08/23	08:38:51	08:48:02	47	70	45	11:04	345	Ingress	1.63	156	1.97
12/09/23	10:09:36	10:10:26	51	73	193	12:38	431	Egress	1.61	157	2.01
19/09/23	03:03:29	03:03:46	46	30	304	08:39	404	Egress	1.61	162	1.96
27/09/23	13:32:12	13:32:44	63	44	206	07:11	414	Egress	1.60	156	1.99
10/10/23	08:46:55	08:56:12	60	38	176	16:23	388	Ingress	1.58	160	2.04
16/10/23	12:08:14	12:18:07	31	36	146	13:51	417	Ingress	1.58	145	1.96
24/10/23	20:49:55	20:50:36	44	−26	83	12:51	351	Egress	1.58	145	1.93
29/10/23	12:52:15	12:52:39	49	−33	244	12:37	316	Egress	1.58	145	1.92
07/12/23	07:17:15	07:18:04	73	24	45	17:01	385	Egress	1.51	129	1.98
11/12/23	09:36:40	09:37:20	64	36	38	16:14	401	Egress	1.51	120	1.94
20/12/23	09:42:17	09:42:34	39	22	96	14:24	399	Egress	1.50	189	1.88
26/03/24	09:19:01	09:28:16	79	17	207	07:08	397	Ingress	1.39	150	1.89
31/03/24	00:17:09	00:17:02	66	−5	168	16:23	376	Egress	1.39	132	1.95
10/04/24	03:42:05	03:41:57	26	−45	157	12:28	305	Egress	1.39	132	2.03
19/04/24	19:44:20	19:45:00	8	−18	11	12:30	377	Egress	1.38	220	1.88
26/04/24	15:08:14	15:08:42	56	34	145	12:25	393	Egress	1.38	169	1.87
08/05/24	03:54:39	03:55:34	36	−22	21	09:24	381	Egress	1.38	208	1.88
15/05/24	08:37:11	08:37:56	54	−70	10	08:39	313	Egress	1.38	216	1.96
31/05/24	17:01:35	17:10:44	57	9	139	15:05	327	Ingress	1.39	184	1.83
17/06/24	19:41:19	19:42:16	35	8	212	11:21	362	Egress	1.39	180	2.17

The profiles are organized chronologically and depict the Martian ionosphere and lower neutral atmosphere under a variety of conditions. The profiles have been shown in order of date as this is inline with changing solar activity. Between 02/04/21 and 27/06/23, the solar cycle was ramping up to maximum. Figure 3 in Withers et al. (2023) also shows vertical profiles with the purpose of comparing solar minimum MAVEN ROSE profiles with solar maximum MGS profiles. So, Figures 2 and 3 can be used in conjunction with this to complete the solar cycle from solar minimum to solar maximum.

With these figures, we are immediately able to determine the behavior of the M2 peak density and altitude with changing SZA and find a clear correlation with increasing SZA, which agrees well with previous work (Fallows et al., 2015; Fox & Weber, 2012; Mendillo et al., 2013; Němec et al., 2011; Sánchez-Cano et al., 2013; Segale et al., 2024). For instance, Panel G of Figure 3 demonstrates the M2 peak altitude rising and its density decreasing as the SZA increases. A more detailed analysis of these profiles will be provided in Section 5.

To validate the profiles before further analysis can take place, a case study for two of these profiles is presented in Figure 4. This figure illustrates the vertical electron densities obtained from measurements conducted on 07/12/22 and 27/06/23, corresponding to panels A and B, respectively. The profile in panel A was selected for its high SZA of 80°, allowing for a direct comparison with conventional RO data. As such, this profile can be compared with both models and instruments. This comparison includes a profile from a MAVEN ROSE measurement taken

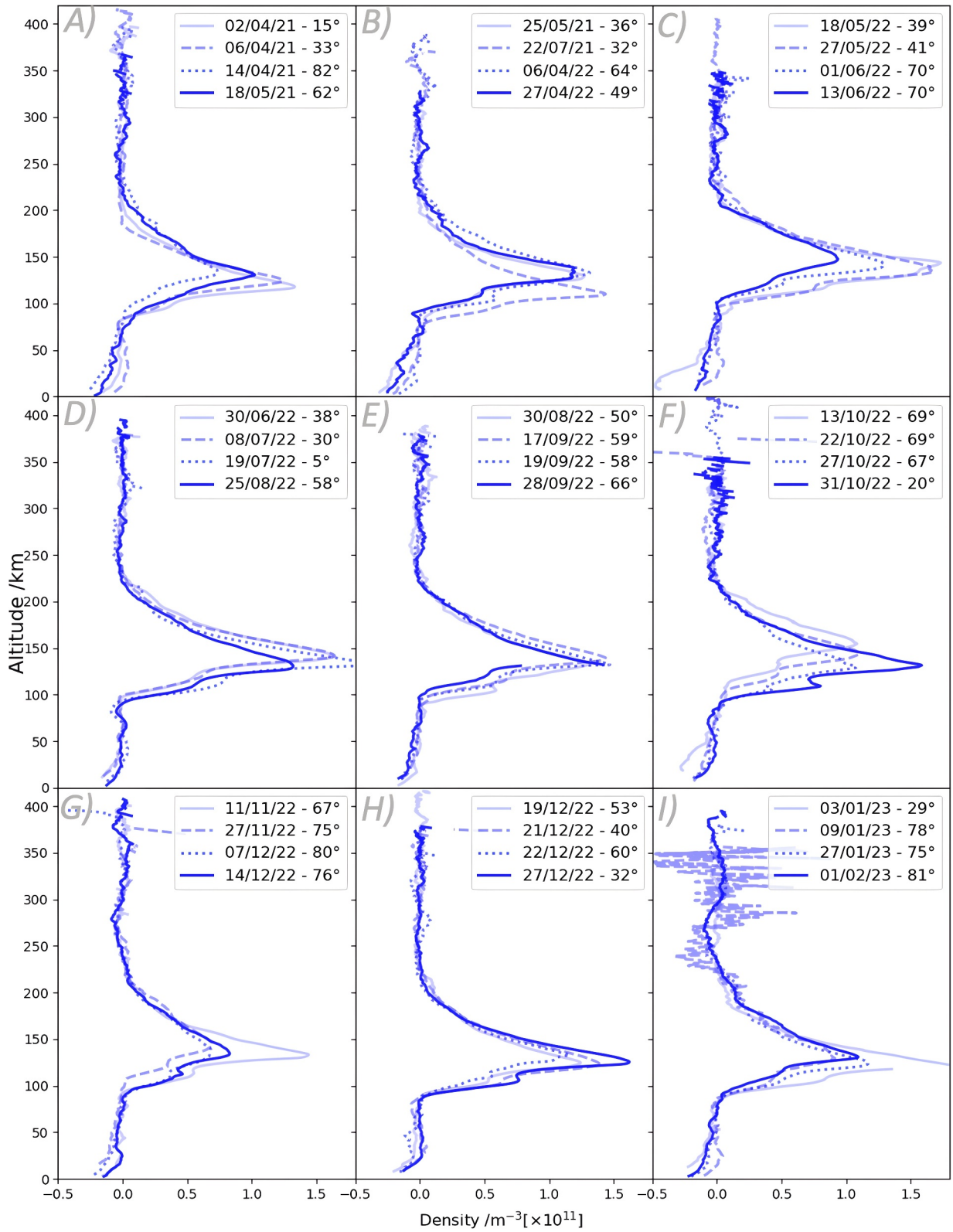

Figure 2. Vertical electron density profiles that have been acquired via mutual radio occultation between Mars Express and Trace Gas Orbiter between 02/04/21 and 01/02/23. As well as the Solar Zenith Angle, the legend for each plot informs when the measurement took place such that it can be checked in Table 1.

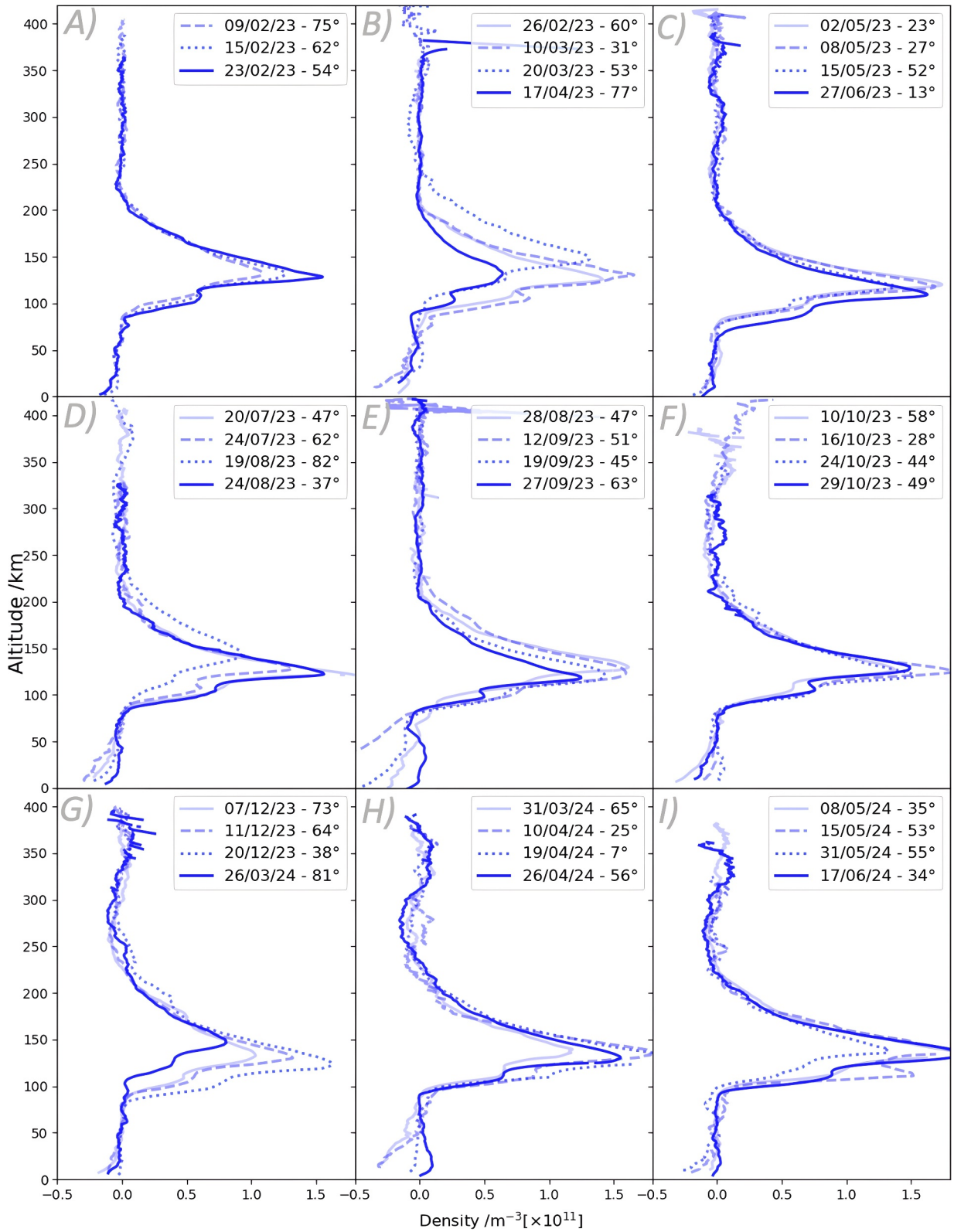

Figure 3. More vertical electron density profiles that have been acquired via mutual radio occultation between Mars Express and Trace Gas Orbiter between 09/02/23 and 17/06/24.

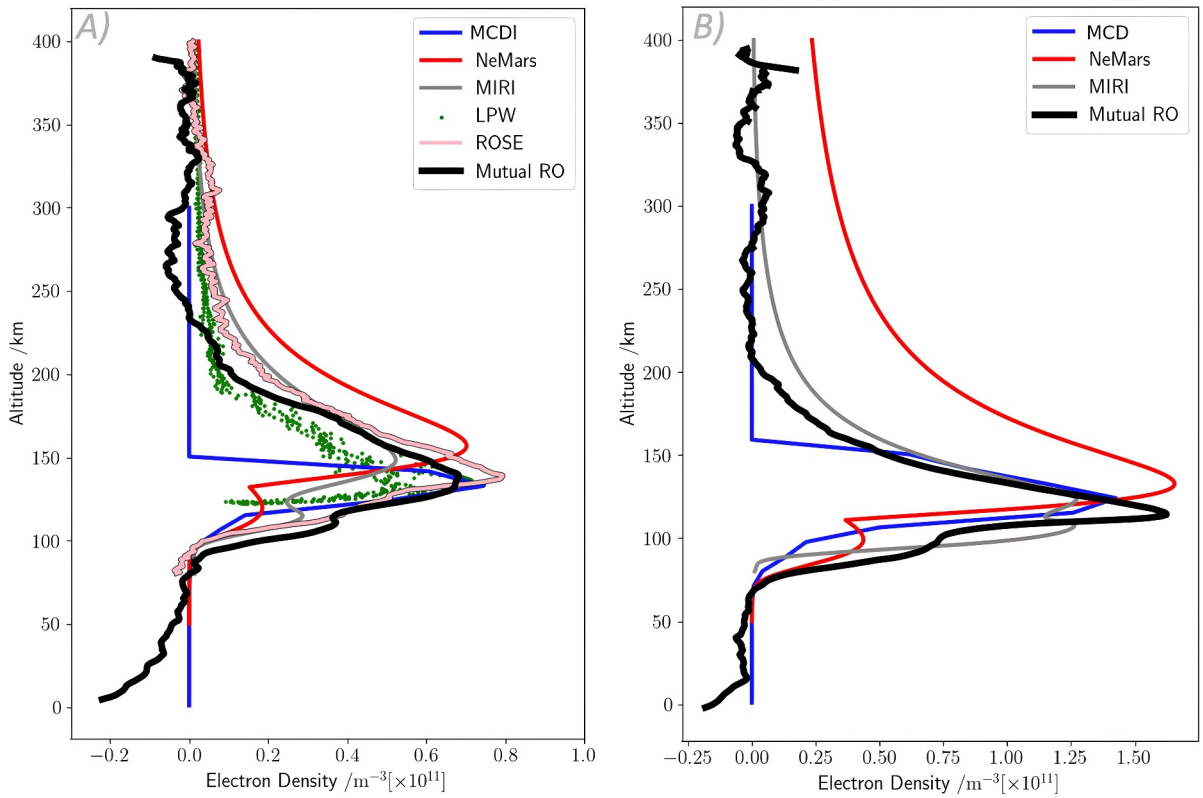

Figure 4. Vertical electron density profiles acquired via mutual Radio Occultation (RO) (black) for the dates of 07/12/22 (Panel A) and 27/06/23 (Panel B). Both profiles are compared with three models: Mars Climate Database, NeMars and Mars Initial Reference Ionosphere. The inputs for all the models are given in 0. Panel B has a measurement from a low solar zenith angle of 13°, and panel A is from a higher angle of 80°, which is more comparable with conventional RO. As such, it has been compared with a MAVEN Radio Occultation Science Experiment measurement. Panel A also includes local measurements from MAVEN's Langmuir Probe and Waves instrument.

under similar conditions, specifically on 07/11/22 at 18:11:18 UT, with a latitude of 44° and an SZA of 80°. Additionally, panel A features a comparison with in-situ electron density measurements from MAVEN's Langmuir Probe and Waves instrument (Andersson et al., 2015), specifically those obtained during Deep-Dip campaign 4 at 08/09/15. This date is very different to the mutual RO data set as MAVEN's orbital parameters mean that it only passes through the low altitude atmosphere during rare deep-dip campaigns. These campaigns have only gone to a low enough altitude around the terminator, so only high SZA comparisons can be made. Unfortunately, this is why such a comparison is not possible for the profile in panel B, as MAVEN has not conducted a deep-dip to the required sub-150 km altitude whilst also having a low SZA.

However, the profile in panel B from 27/06/23 is from such a low SZA (13°) that there are no instruments that it can be compared with and can only be shown against models. These have been included to further provide validity to the mutual RO results and the inputs to these models, such as SZA and irradiance, can be found in Table 1. The Mars Climate Database (MCD) Global Circulation Model (MCD) provides the most comprehensive prediction due to its inclusion of atmospheric and heliophysical dynamics (Forget et al., 1999; González-Galindo et al., 2013; Millour et al., 2022), although it is constrained by resolution limitations and the absence of an M1 layer. Whilst the MCD profiles might seem sparse, the specific values for M2 altitude and peak density should be considered the most accurate among the other two models. The NeMars model is an empirical model derived from data collected by MEX's Mars Advanced Radar for Subsurface and Ionosphere Sounding (MARSIS) experiment, as well as conventional RO data from the MGS (Sánchez-Cano et al., 2013). The Mars Initial Reference Ionosphere (MIRI) model (Mendillo et al., 2013), which primarily relies on MARSIS data and incorporates some conventional RO data from MGS, also serves as a comparative framework. Additionally, the MIRI model includes data from the Mars Express Radio Science (MaRS) experiment (Pätzold et al., 2004). As a semi-empirical model, MIRI's numerical parameterizations are informed by well-established physical principles governing ionospheric behavior.

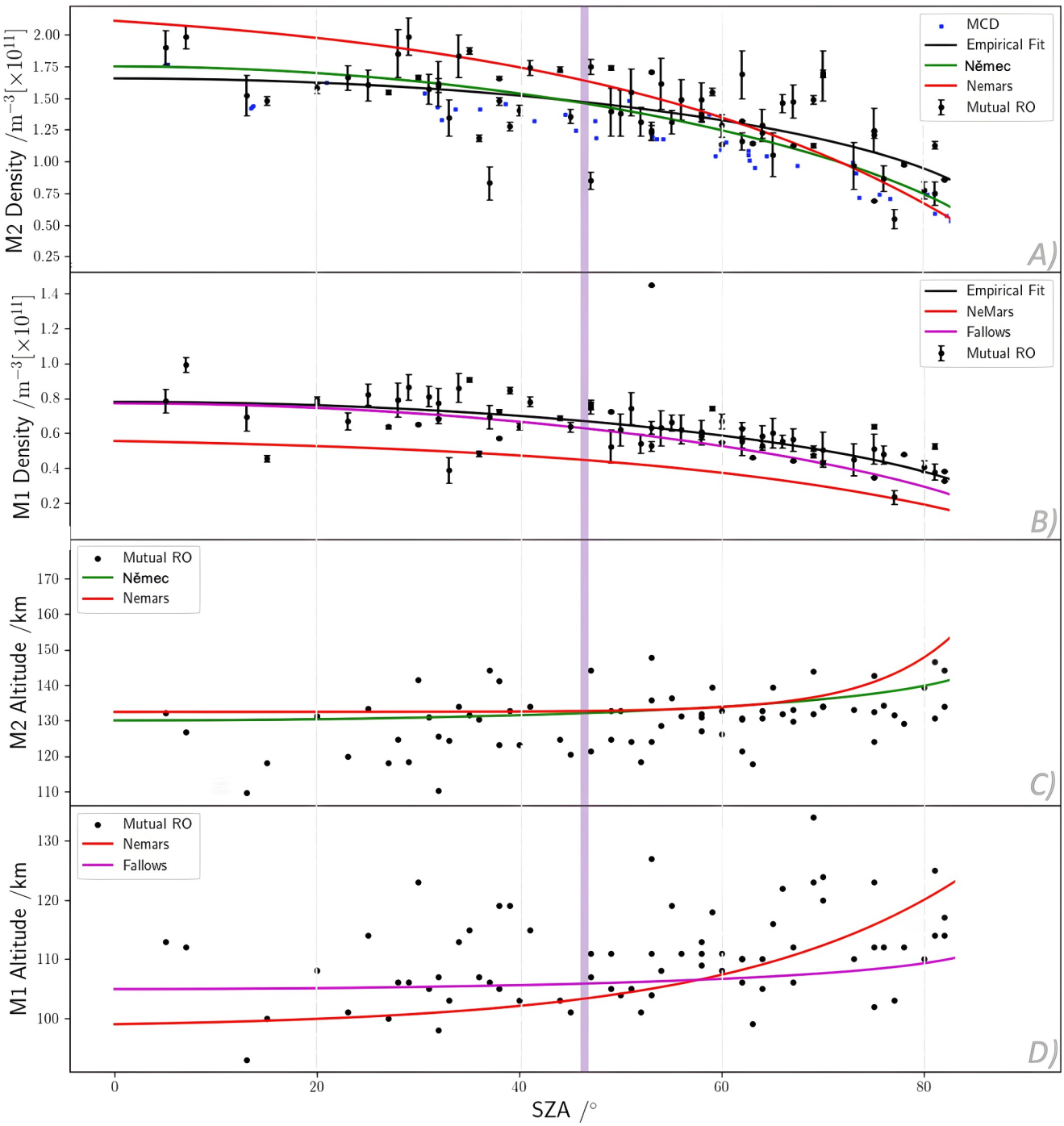

Figure 5. The variability of four key ionospheric parameters with increasing Solar Zenith Angles. Panel (a) indicates the M2 electron density, blue stars shows the density if the time and location for each measurement were input into a Mars Climate Database Global Circulation Model, the black lines are the empirical fits (explained in the text), the green line is the trend found in Němec et al. (2011), the red line is that of the NeMars model (Sánchez-Cano et al., 2013) and the purple is the fit from Fallows et al. (2015).

4. Results

The SZA trends in altitude and peak density for the M1 and M2 ionospheric layers are illustrated in Figure 5, derived from the profiles presented in Figures 2 and 3. As noted by Withers et al. (2024), the lowest SZA RO profiles obtained on Mars occur at 45°, indicated by a purple demarcation in the figure. This highlights the

advantage of this mutual RO method, revealing 34 measurements that would be unattainable using conventional RO techniques. The error bars represent 1 standard deviation, and have been calculated in the same way as those in Parrott et al. (2024), in that each data set was processed 100 times with a 5% of the max amplitude input as stochastic noise. Error bars are not visible for panel C and D as altitude readings in our technique are very accurate. Height-error is a combination of spatial error from the SPICE framework ($\ll$1 km) and the Electra/MELACOM on/off commanding time (<1 s).

Each of the four panels is compared with the NeMars model, with the inputs listed in Table 1. An alternative empirical fit for these M2 trends is also provided by Němec et al. (2011), based on MARSIS data. They observed that the M2 density is better represented by an inverse exponential decay rather than the conventional flattened cosine function. Both of these models focused on the entire ionospheric structure, but Fallows et al. (2015) specifically focused on the M1 trend (found through MGS conventional RO profiles), so their trend can also be found in Figure 5.

Additionally, the MCD is utilized for comparison. The inputs for this are detailed in Table 1, include date, time, and coordinates, enabling the calculation of SZA, solar distance, season, solar activity, and atmospheric state; so this model should be regarded as the most accurate for M2 peak densities. However, it does not include a representation of the M1 layer and suffers from low vertical resolution. Consequently, it is not employed in panel B, which examines M2 altitude, as the model restricts the M2 peak altitude to only four discrete altitudes.

Having outlined the models, we now turn to the panel descriptions in descending order. Panel A of Figure 5 depicts the M2 density trend as a function of SZA, following the empirically fit relation of $1.6 \times 10^5 \times \cos\mathrm{SZA}^{-0.25}$. All models used here, except the model of Němec et al. (2011), have trends that follow a similar flattened cosine morphology, although the MCD exhibits a narrower spread, suggesting that peak densities are modulated by factors not accounted for in the MCD. However, both the mutual RO and MCD data shows some amount of spread. A key reason for this could be the dawn/dusk symmetry mentioned earlier in this article.

Panel B illustrates the same trend for the M1 layer. An initial conclusion can be made about the presence of the M1 ionospheric layer, which was expected to not exist during the midday (Mayyasi & Mendillo, 2015), but was predicted recently by Segale et al. (2024). A notable anomaly occurs when SZA is 53°, with a density of 1.51×10^{11} m^{-3}, recorded at 08:37 on 15/05/24, shortly after a solar flare and during a coronal mass ejection disturbance. This significant result is outside the scope of this publication and merits a dedicated publication. This panel is particularly significant as it represents the first examination of the M1 layer in low-SZA regions.

Panel C presents the M2 altitude trend, with both models predicting a slight growth with SZA, which only begins to rise substantially around 70° SZA.

Lastly, panel D focuses on M1 altitude, which exhibits the greatest variability among these trends and shows minimal correlation with SZA. The highest M1 altitude is observed at 82°, while the lowest is at 15°, which agrees with theory (Fallows et al., 2015; Fox & Weber, 2012; Mendillo et al., 2013; Němec et al., 2011; Sánchez-Cano et al., 2013; Segale et al., 2024). This wide spread around the theoretical trend has reduced the value of showing any empirical fit. The model in Němec et al. (2011) does not provide a fit for M1 altitudes and the NeMars models are expected to perform poorly in predicting this variable for low SZA, as they are partially based on MARSIS data, which, due to its radar sounder nature, cannot penetrate below the higher M2 layer. They also assimilate MGS RO data, but is confined to high SZA, making the low SZA predictions speculative.

5. Discussion

5.1. Solar Driven Ionospheric Variability

Numerous studies have analyzed how martian ionospheric layers vary with SZA (Hantsch & Bauer, 1990; Morgan et al., 2008; Němec et al., 2011; Zhang et al., 1990). However, the mutualRO data set marks a significant shift from focusing solely on high SZA values, necessitating an update to the empirical formulas to ensure their validity in low SZA regions. The following density formulas for the M1 and M2 ionospheric layers are presented, with irradiance represented by either $F_{10.7}$ or F_{EUV}, measured in solar flux units and mWm^{-2}, respectively. The latter is preferred due to its higher accuracy, as it uses a frequency band more relevant to ionospheric formation. These irradiance levels, derived from the 43 and 59.5 nm bands of the FISM2 model (Chamberlin et al., 2020),

were chosen because they closely match the ionization cross-sections of CO_2 (as shown in Figure 10 of Lollo et al., 2012). On the other hand, $F_{10.7}$ is included for comparability with previous empirical fits, even though it is measured for Earth at a different radio frequency band. Below are the empirical fits for the M1 and M2 electron densities, expressed in terms of F_{EUV} or $F_{10.7}$.

$$N_{M2} = 1.6 \times 10^{11} \cos(\mathrm{SZA})^{-0.25} + 4.3 \times 10^{8} F_{10.7} \quad (2)$$

$$= 1.6 \times 10^{11} \cos(\mathrm{SZA})^{-0.25} + 5.3 \times 10^{10} F_{EUV} \quad (3)$$

$$N_{M1} = 7.3 \times 10^{10} \cos(\mathrm{SZA})^{-0.34} + 2.5 \times 10^{8} F_{10.7} \quad (4)$$

$$= 7.3 \times 10^{10} \cos(\mathrm{SZA})^{-0.34} + 3.1 \times 10^{10} F_{EUV} \quad (5)$$

Equations 2 and 4 were derived using the same methodology as Němec et al. (2011), where the largest factor (SZA) was determined first, followed by the calculation of the Spearman rank coefficient on the residuals for subsequent minor parameters until the correlation fell below 0.2. This analysis yielded a surprising result: solar distance played a negligible role in influencing electron densities, with correlations of −0.16 for M2 and −0.01 for M1. This is evident in Figure 6, where the effects of solar distance (shown in the panel C) show no resemblance to the sub-solar peak density values. In contrast, increasing solar activity (indicated by $F_{10.7}$ and FISM-2 data) is correlated with rising sub-solar values. The low correlations observed are likely due to the limited sample size.

As described in Section 2, the M1 layer is primarily driven by impact soft X-ray photoionization. Therefore, it may be more appropriate to examine the correlation with weaker soft X-ray irradiance levels. Instead of using the aforementioned EUV bands, the average of the 0.225, 0.6, 1.3, and 2.5 nm bands was utilized. This led to a coefficient of 2.27×10^{11} with a correlation of 0.61, which is a slight improvement over F_{EUV}, which had a correlation of 0.58.

The SZA coefficient found here is notably lower than those reported in previous studies. The value of −0.25 produces a much flatter SZA trend for M2 densities. Hantsch and Bauer (1990), using Viking Lander and Mariner 4 data, predicted a coefficient of −0.57. Fox and Yeager (2006), using MGS occultation data, found a coefficient of −0.49 for periods of high solar activity. Morgan et al. (2008) refined the coefficient to −0.476 using a large data set from MARSIS AIS, which populated the low-SZA region. The lower coefficients obtained from mutual RO are likely because previous estimates have been primarily based on conventional RO, which lacks data for low-SZA regions and requires extrapolation to these lower SZA values. The only substantial data for midday comes from MARSIS AIS, which systematically produces higher topside density readings. Consequently, the inclusion of radar sounding data leads to an overestimation of midday density values and, overall, a steeper cosine trend with a larger SZA coefficient.

The M1 layer has been less extensively studied. However, Fox and Yeager (2006) used MGS conventional RO measurements from high-SZA regions and found a cosine exponent of −0.55 for low solar activity and −0.53 for high solar activity. The fact that the M1 SZA coefficient is larger than that of M2 is noteworthy. This is likely due to the greater penetration depth of soft X-rays, meaning the ionization occurs at altitudes where the neutral atmosphere is denser. As the slant angle increases during the day, moving away from the sub-solar point, the integral density rises at a faster rate than if the flux were at the same angle at a higher altitude. This steeper rate of ionization results in a larger SZA cosine coefficient.

Estimates of the sub-solar M2 peak density value lie in the middle range of previous estimates. The most accurate estimates are obtained via MARSIS radar sounding instruments, which consistently access low-SZA regions and do not require extrapolation from near the terminator. However, estimates by different authors using the same instrument vary widely due to the period at which their measurements were taken, including 2.1×10^{11}, 2.0×10^{11}, 1.8×10^{11}, and 1.6×10^{11} m^{-3} from Safaeinili et al. (2007), Gurnett et al. (2008), Nielsen et al. (2006), and Morgan et al. (2008), respectively. Only the last estimate agrees with the value obtained via mutual RO, as radar sounding tends to predict higher electron densities than RO.

Empirical fits were also determined for the altitudes of both ionospheric layers. The small sample size significantly limited the confidence levels, as indicated by the low correlation levels and the spread around the fits in

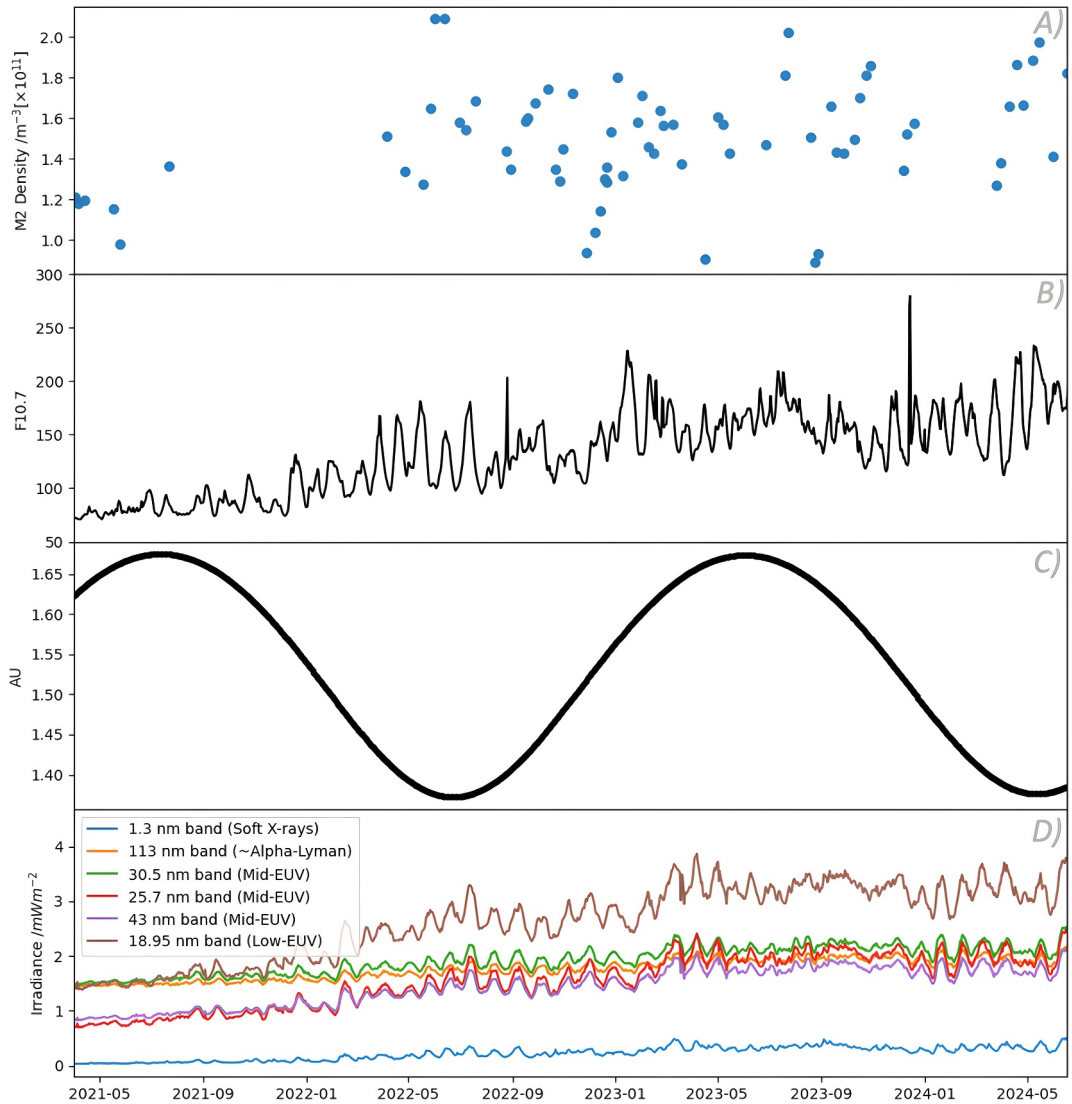

Figure 6. Sub-Solar M2 Peak Electron Densities [corrected using $1.6 \times 10^{11} \cos(\mathrm{SZA})^{-0.25}$] compared with three major driving forces. Panel (b) shows the $F_{10.7}$ irradiance levels measured at Earth. Panel (c) is the martian solar distance measured in AU. Panel is irradiance levels simulated using the FISM-2 Model to 1AU.

Figure 5. Consequently, the fitted model was kept relatively simple, with SZA being the only significant factor. The first equation describing the altitudes of the M2 ionospheric layer was developed by Hantsch and Bauer (1990) and follows the form $h_m = h_0 + H \ln(\sec(\mathrm{SZA}))$, where h_0 is the sub-solar altitude and H is the scale height. The empirical fits are as follows:

$$h_{M2} = 125.9 + 5.9 \ln(\sec(\mathrm{SZA})) \quad (6)$$

$$h_{M1} = 106.2 + 5.3 \ln(\sec(\mathrm{SZA})) \quad (7)$$

5.2. Neutral Temperature Trend

As described in Appendix A2, the neutral temperatures can be inferred by the scale height of the M2 ionospheric peak. With this, a trend for the neutral temperature around the M2 ionospheric peak with increasing SZA can be found in Figure 7, which shows a temperature gradient of around 0.46 K per degree of SZA.

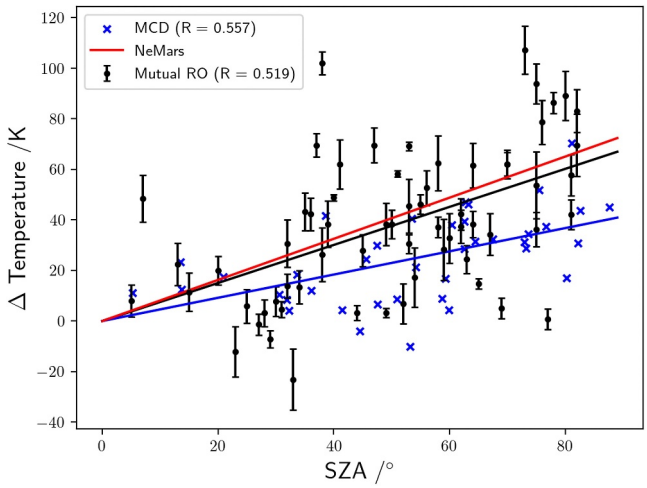

Figure 7. Temperature trend with solar zenith angle. Blue stars are the from the same empirical Chapman fit method described in Appendix A2, but applied to the profiles found via the Mars Climate Database Global Circulation Model. The red line is the same method applied but for profiles derived from the NeMars model.

Similar to the approach used for Figure 5, error bars have been calculated in the same way, and the same MCD has been employed for comparison. The inputs for this are derived from the time and coordinates of each mutual RO measurement, ensuring consistency in SZA, solar activity, and solar distance, with variations in season and atmospheric circulation. Although the NeMars model was not originally intended to provide insights into neutral temperatures, it has been included here due to its ability to explicitly output ionospheric scale height, which can then be utilized in Equation A2.1 to estimate neutral temperatures.

Both the data and the two models have been normalized by bringing the initial value to 0 K, recognizing that these models rely heavily on MARSIS data for low SZA regions, as it represents the most extensive data set for these midday local times (Vogt et al., 2016). However, due to the fundamentally different measurement techniques and processing, the values needed to be normalized with a temperature offset of 202 K, 139 K, and 236 K for our measurements, the MCD, and NeMars, respectively.

The results depicted in Figure 7 may initially seem counter-intuitive, given that conventional understanding suggests a decrease in temperature with an increase in SZA due to reduced insolation. The increased slant angle causes solar flux to penetrate less deeply, resulting in a reduced deposition of thermal energy in the atmosphere around the M2 peak.

One might also hypothesize that, given the M2 altitudes are situated within the lower thermosphere, temperatures would be expected to rise with altitude. Furthermore, as Figure 5 illustrates, atmospheric layers are anticipated to ascend with increasing SZA. Despite this, an analysis of the 71 available profiles revealed no correlation between M2 peak altitude and temperature.

A comparable trend was observed by Jain et al. (2023), using data from MAVEN's Imaging Ultraviolet Spectrograph instrument (McClintock et al., 2015), although at a considerably higher altitude of 170–180 km. They proposed that temperature increases steadily throughout the Martian day, with heat only dissipating beyond the dusk terminator.

The temperature dynamics in this region have previously been explored through simulations by Bougher and Shinagawa (1998) using the Mars Thermosphere General Circulation Model (MTGCM), where their simulation results showed an increase in temperature with SZA. However, their study did not provide a detailed explanation for why this temperature trend occurred.

Using the more advanced and modern MCD, we have simulated transport processes at various altitudes. The outcomes of these simulations are presented in Figure 8. The MCD was used for the Martian spring equinox (Solar Longitude = 0°) with the meridian set to local time 18:00, placing the sub-solar point (12:00) at approximately 90° longitude.

The left column of Figure 8 displays temperature, and it shows the warmest regions are observed near the poles and the terminator around 18:00. This temperature distribution can be employed to validate the results obtained via mutual RO in Figure 7, which showed that the temperature should increase as we get further away from the subsolar point at 12:00. Please note, the local times appear to be counting backwards across the *x*-axis, this is to account for the rotational direction of Mars' spin. This complex dynamic has also been depicted in Figure 9 to aid understanding. The right column depicts the magnitude and direction of horizontal winds as a quiver map, superimposed on a map showing the scalar value of downward wind. At an altitude of 200 km, the simulation reveals divergent winds originating from approximately 19:00 local time. The divergence does not originate at the sub-solar point due to the time lag required for the low-density atmosphere to warm. These divergent winds accelerate toward the poles, becoming transpolar, crossing over to the night side, and converging on the other side of the planet. The MTGCM also found these high-altitude transpolar winds in 1998 (Bougher & Shinagawa, 1998). The convergent winds gather around 08:00 leading to downwelling. This, in turn, causes divergent winds at lower altitudes near this antisolar point. Overall, the simulation illustrates divergent winds on the night side around 120 km due to downwelling near the anti-solar point, as well as divergent winds on the day side

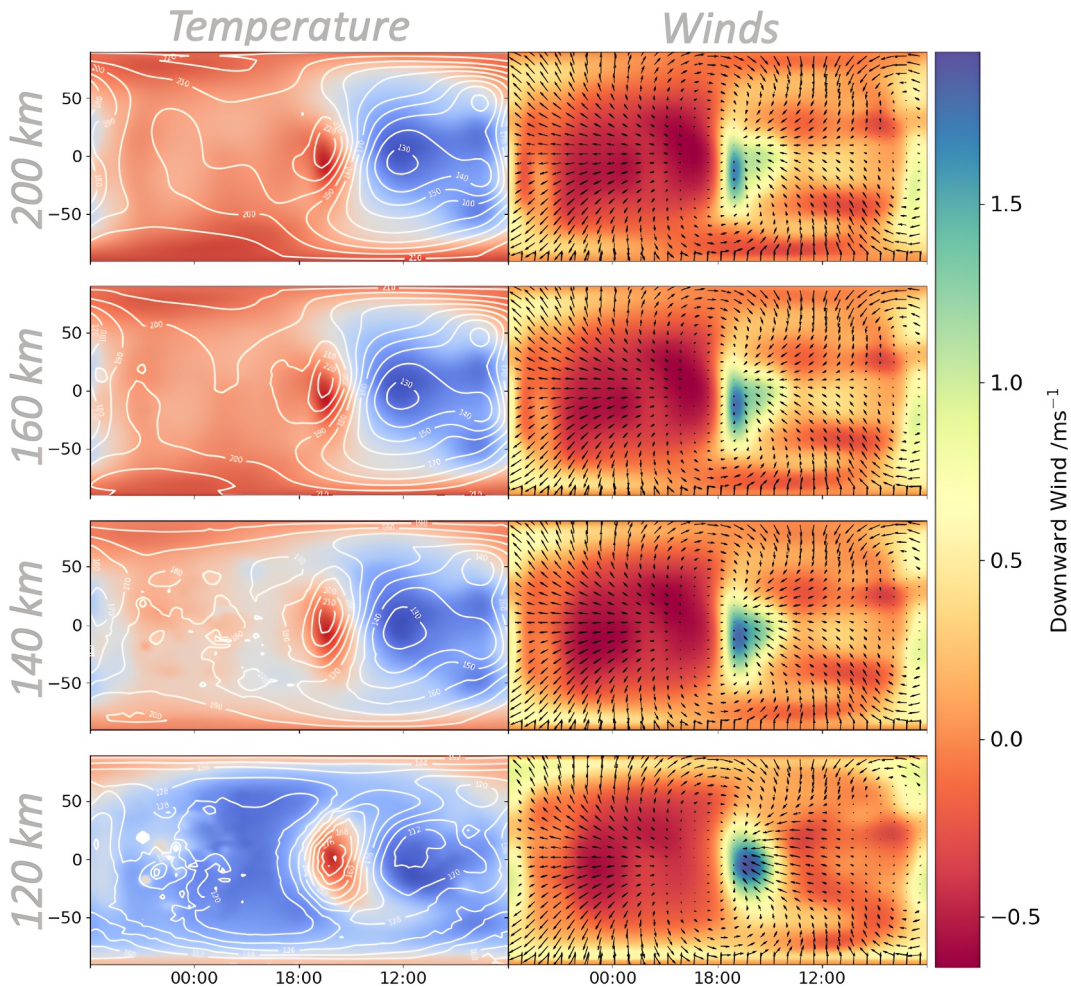

Figure 8. Mars Climate Database simulation results of the global thermospheric temperatures and wind at altitudes 120–200 km. Local times seem to be in reverse order, this is to match latitude with local times and to account for the direction of rotation of Mars. The dusk terminator is leading up to 18:00, and can be seen by the downwelling in the wind map and the warmer region in the temperature map.

resulting from solar heating. These dynamics result in winds converging near the terminator, accompanied by further downwelling. The observed higher temperatures are attributed to the adiabatic heating of air as it descends to lower altitudes.

In summary, this MCD simulation explains why there are divergent winds originating from the antisolar point. When these winds coming from the nightside collide with winds from the dayside (driven by solar heating), they are diverted downwards and warm-up as the air parcels are compressed as the pressure increases with decreasing altitude.

6. Conclusions

This study presents a detailed analysis of the martian ionosphere using mutual RO observations, showcasing 71 full vertical profiles out of a total of 124 measurements. Notably, 35 of these measurements were conducted in SZA regions lower than previously explored, offering new insights into the martian ionosphere. This expanded SZA coverage is a distinct advantage of mutual RO over conventional RO, and unlike radar sounders it includes whole vertical profile of the ionosphere, allowing for a more comprehensive understanding of atmospheric and ionospheric dynamics.

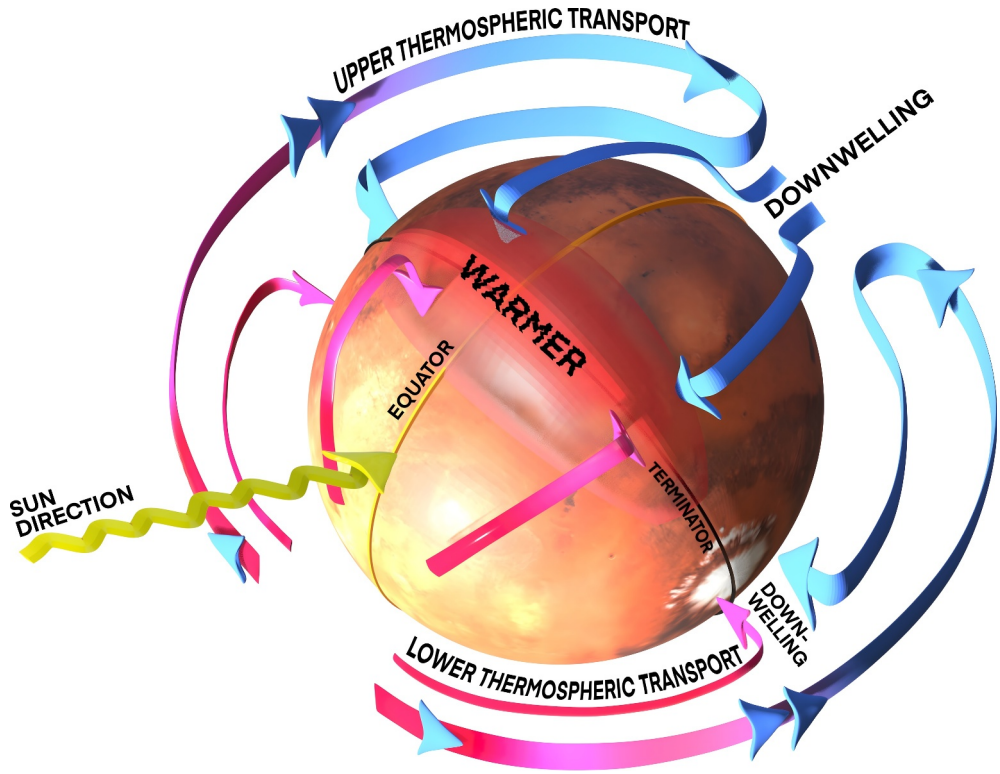

Figure 9. A cartoon showing the cause of the increasing temperature as the Solar Zenith Angle increases near the equator. This is due to high altitude trans-polar winds causing divergent nightside winds around 120 km. The subsolar point is intentionally 50° of the divergent region, to account for the time required for solar heating.

This article has also explored the trends of the peak electron densities and altitudes of both the M2 and M2 ionospheric layers. Finding similar cosine trends to previous studies, but finding that the M2 peak density should change less dramatically during the day. This was inferred by the cosine coefficient −0.25, which is about half the predictions in other works. This is likely due to our midday data sets which previous authors have not had access to. Empirical fits for altitudes where also provided, but the spread around this trend is significant as it is likely held back by the small data set size. For both fits, irradiance has been factored in as $F_{10.7}$ and F_{EUV}. The former to align with previous works, and the latter due to the ionospheres sensitivity to this specific frequency band.

Additionally, this study extracted neutral temperature values from the derived vertical profiles. This revealed a thermospheric temperature increasing with SZA. This counter-intuitive result was explored with MCD simulations to reveal the dynamics are circulation driven, instead of being due to solar heating.

In conclusion, this research not only advances our understanding of the Martian ionosphere but also demonstrates the value of mutual RO as a powerful tool for thermospheric studies. The findings may have important implications for future missions and research, providing a solid foundation for further exploration of Mars and potentially other planetary bodies with similar observational techniques.

Appendix A

A1. Processing Chain Amendment

Several techniques have been implemented to extract valuable information from the raw data sets collected by TGO's Electra antenna. However, a significant enhancement has been introduced to improve the reliability of the final vertical electron density profiles. Specifically, Steps 4 and 5 in the Processing section of Parrott et al. (2024) outlined two procedures designed to account for variable frequency drift caused by the unstable oscillator. The initial step involves fitting a polynomial of variable order to the "vacuum portion" of the residuum, ensuring it

closely approximates the data and intersects at the point where the ionosphere and neutral atmosphere counteract, producing a gradient of 0 Hzs^{-1}. The subsequent step entails iteratively applying an increasing linear frequency bias during the inverse Abel transform until the electron density in the 70–80 km region of the resultant vertical profile is minimized to near zero.

However, this linear bias introduced errors, as its magnitude increased over time, leading to significant discrepancies toward the end of the measurement. These errors often manifested as artificially high electron densities in the lower neutral atmosphere, sometimes exceeding the M2 peak density.

To address this issue, the two steps have been consolidated into a single process, thereby eliminating the need for the linear bias stage. The polynomial detrend's effectiveness is now validated by minimizing the electron density in the 70–80 km region after the Abel inversion. The revised approach involves adjusting the polynomial detrend to account for the oscillator drift in the "vacuum portion" of the residuum, while allowing for a small offset from the 0 Hzs^{-1} point—up to ±0.5 Hz. This offset is determined through an optimization algorithm that iteratively adjusts the value until the same physically realistic low electron density is achieved in the 70–80 km region.

A2. Finding Neutral Temperatures Near the M2 Layer

Neutral temperatures at M2 altitudes can be determined through the analysis of the scale height in vertical electron density profiles. This method is valid because this region of the atmosphere is at photochemical equilibrium, where the timescales for transport are significantly longer than those for photochemical production and loss processes (Withers, 2009). The underlying logic is as follows: as the neutral atmosphere warms, it expands, causing the optical depth of unity to be reached at higher altitudes by the incident solar flux. This results in peak photoionization occurring at elevated heights. However, since the solar flux itself remains constant, the peak electron density does not change. Consequently, the ionospheric layers exhibit an increased scale height H, which can be readily determined.

The process begins by parametrically fitting Equation 1 to the M2 peak, following the approach outlined by Sánchez-Cano et al. (2016). However, regions significantly above the M2 peak are no longer in photochemical equilibrium due to the dominance of transport dynamics, and regions below the M2 peak coincide with the M1 ionospheric layer. Therefore for this analysis, the parametric fit is performed within a range of −20 to +50 km around the M2 peak, ensuring a reliable estimation of the scale height H.

The scale height H can then be used to calculate the neutral temperature T_n using the following equation:

$$T_n = \frac{Hgm}{k} \tag{A2.1}$$

where m is the molecular mass of CO_2, k is the Boltzmann constant, and gravity g is dependent on altitude, calculated as:

$$g = G\frac{M}{(r_m - h)^2} \tag{A2.2}$$

Here, G represents the Martian gravitational acceleration of 6.67×10^{-11} $m^3kg^{-1}s^{-2}$, r_m is the mean Martian radius of 3.338×10^6 m, and h corresponds to the M2 altitude.

Data Availability Statement

All data required has been provided in the ESA Guest Storage Facility (Parrott, 2024). This includes the data for Table 1, and the data products for multiple steps along the processing chain to acquire the vertical electron density profiles. A data product guide has been provided to assist. The products exist for each of the mutual RO measurements shown, and they are:

1. Beginning with the In-phase and Quadrature representation of the waveform received at TGO's Electra antenna.
2. The net Doppler shift in the signal.

3. A simulation with SPICE for the Doppler shift produced by the relative motion of the two spacecraft.
4. The difference between the net Doppler shift and the SPICE simulation. This is the frequency shift due to the Martian atmosphere, modulated by the effects of the Electra unstable oscillator.
5. The residuum, this is the frequency shift due to the atmosphere once the instabilities have been correct for.
6. Vertical refractivity profile acquired via the inverse-Abel transform.
7. Vertical electron density profile.

Acknowledgments
J.P acknowledges his UK Science and Technology Facilities Council (STFC) Ph. D. Bursary ST/T506151/1 and the ongoing support of the ESA Science Operations Centre and Mission Operations Centre teams. He also thanks Kingdom Parrott for their creation of Figure 9. IMW is grateful for the support from UK-STFC grant ST/S000364/1. B.S.-C. acknowledges support through UK-STFC Ernest Rutherford Fellowship ST/V004115/1.

References

Andersson, L., Ergun, R. E., Delory, G. T., Eriksson, A., Westfall, J., Reed, H., et al. (2015). The Langmuir probe and waves (LPW). *Instrument for MAVEN*, *195*(1–4), 173–198. https://doi.org/10.1007/s11214-015-0194-3

Andrews, D. J., Stergiopoulou, K., Andersson, L., Eriksson, A. I. E., Ergun, R. E., & Pilinski, M. (2023). Electron densities and temperatures in the Martian ionosphere: MAVEN LPW observations of control by crustal fields. *Journal of Geophysical Research: Space Physics*, *128*(2). https://doi.org/10.1029/2022ja031027

Ao, C. O., Edwards, C. D., Kahan, D. S., Pi, X., Asmar, S. W., & Mannucci, A. J. (2015). A first demonstration of Mars crosslink occultation measurements. *Radio Science*, *50*(10), 997–1007. https://doi.org/10.1002/2015rs005750

Bougher, S. W., & Shinagawa, H. (1998). The Mars thermosphere-ionosphere: Predictions for the arrival of Planet-B. *Earth Planets and Space*, *50*(3), 247–257. https://doi.org/10.1186/bf03352111

Chamberlin, P. C., Eparvier, F. G., Knoer, V., Leise, H., Pankratz, A., Snow, M., et al. (2020). The flare irradiance spectral model-version 2 (FISM2). *Space Weather*, *18*(12). https://doi.org/10.1029/2020sw002588

Fallows, K., Withers, P., & Matta, M. (2015). An observational study of the influence of solar zenith angle on properties of the m1 layer of the mars ionosphere. *Journal of Geophysical Research: Space Physics*, *120*(2), 1299–1310. https://doi.org/10.1002/2014JA020750

Felici, M., Withers, P., Smith, M. D., González-Galindo, F., Oudrhiri, K., & Kahan, D. (2020). Maven rose observations of the response of the martian ionosphere to dust storms. *Journal of Geophysical Research: Space Physics*, *125*(6), e2019JA027083. https://doi.org/10.1029/2019JA027083

Felici, M., Withers, P., Vogt, M. F., Hensley, K. G., & Andersson, L. (2022). Electron densities in the ionosphere of mars: Comparison of maven/rose and maven/lpw measurements. *Journal of Geophysical Research: Space Physics*, *127*(4), e2021JA030155. https://doi.org/10.1029/2021JA030155

Fjeldbo, G., Kliore, A. J., & Eshleman, V. R. (1971). The neutral atmosphere of venus as studied with the mariner v radio occultation experiments. *The Astronomical Journal*, *76*, 123. https://doi.org/10.1086/111096

Fjeldbo, G., Sweetnam, D., Brenkle, J., Christensen, E., Farless, D., Mehta, J., et al. (1977). Viking radio occultation measurements of the Martian atmosphere and topography: Primary mission coverage. *Journal of Geophysical Research (1896-1977)*, *82*(28), 4317–4324. https://doi.org/10.1029/JS082i028p04317

Forget, F., Hourdin, F., Fournier, R., Hourdin, C., Talagrand, O., Collins, M., et al. (1999). Improved general circulation models of the Martian atmosphere from the surface to above 80 km. *Journal of Geophysical Research*, *104*(E10), 24155–24176. https://doi.org/10.1029/1999JE001025

Fox, J. L. (2004). Response of the Martian thermosphere/ionosphere to enhanced fluxes of solar soft X rays. *Journal of Geophysical Research*, *109*(A11). https://doi.org/10.1029/2004ja010380

Fox, J. L., Brannon, J. F., & Porter, H. S. (1993). Upper limits to the nightside ionosphere of mars. *Geophysical Research Letters*, *20*(13), 1339–1342. https://doi.org/10.1029/93GL01349

Fox, J. L., Johnson, A. S., Ard, S. G., Shuman, N. S., & Viggiano, A. A. (2017). Photochemical determination of O densities in the Martian thermosphere: Effect of a revised rate coefficient. *Geophysical Research Letters*, *44*(16), 8099–8106. https://doi.org/10.1002/2017gl074562

Fox, J. L., & Weber, A. J. (2012). Mgs electron density profiles: Analysis and modeling of peak altitudes. *Icarus*, *221*(2), 1002–1019. https://doi.org/10.1016/j.icarus.2012.10.002

Fox, J. L., & Yeager, K. E. (2006). Morphology of the near-terminator Martian ionosphere: A comparison of models and data. *Journal of Geophysical Research*, *111*(A10), A10309. https://doi.org/10.1029/2006ja011697

Girazian, Z., Luppen, Z., Morgan, D. D., Chu, F., Montabone, L., Thiemann, E. M. B., et al. (2020). Variations in the ionospheric peak altitude at mars in response to dust storms: 13 years of observations from the mars express radar sounder. *Journal of Geophysical Research: Planets*, *125*(5), e2019JE006092. https://doi.org/10.1029/2019JE006092

Girazian, Z., Mahaffy, P., Lillis, R. J., Benna, M., Elrod, M., Fowler, C. M., & Mitchell, D. L. (2017a). Ion densities in the nightside ionosphere of Mars: Effects of electron impact ionization. *Geophysical Research Letters*, *44*(22), 11248–11256. https://doi.org/10.1002/2017GL075431

Girazian, Z., Mahaffy, P. R., Lillis, R. J., Benna, M., Elrod, M., & Jakosky, B. M. (2017b). Nightside ionosphere of Mars: Composition, vertical structure, and variability. *Journal of Geophysical Research (Space Physics)*, *122*(4), 4712–4725. https://doi.org/10.1002/2016JA023508

González-Galindo, F., Chaufray, J., López-Valverde, M. A., Gilli, G., Forget, F., Leblanc, F., et al. (2013). Three-dimensional Martian ionosphere model: I. The photochemical ionosphere below 180 km. *Journal of Geophysical Research (Planets)*, *118*(10), 2105–2123. https://doi.org/10.1002/jgre.20150

Gupta, N., Venkateswara Rao, N., & Kadhane, U. R. (2019). Dawn-dusk asymmetries in the Martian upper atmosphere. *Journal of Geophysical Research: Planets*, *124*(12), 3219–3230. https://doi.org/10.1029/2019JE006151

Gurnett, D., Huff, R., Morgan, D., Persoon, A., Averkamp, T., Kirchner, D., et al. (2008). An overview of radar soundings of the Martian ionosphere from the Mars Express spacecraft. *Advances in Space Research*, *41*(9), 1335–1346. https://doi.org/10.1016/j.asr.2007.01.062

Hanson, W. B., Sanatani, S., & Zuccaro, D. R. (1977). The Martian ionosphere as observed by the Viking retarding potential analyzers. *Journal of Geophysical Research*, *82*(B28), 4351–4363. https://doi.org/10.1029/JS082i028p04351

Hantsch, M., & Bauer, S. (1990). Solar control of the Mars ionosphere. *Planetary and Space Science*, *38*(4), 539–542. https://doi.org/10.1016/0032-0633(90)90146-h

Hinson, D. P., Simpson, R. A., Twicken, J. D., Tyler, G. L., & Flasar, F. M. (1999). Initial results from radio occultation measurements with mars global surveyor. *Journal of Geophysical Research*, *104*(E11), 26997–27012. https://doi.org/10.1029/1999JE001069

Jain, S., Soto, E., Evans, J., Deighan, J., Schneider, N., & Bougher, S. (2023). Thermal structure of Mars' middle and upper atmospheres: Understanding the impacts of dynamics and solar forcing. *Icarus*, *393*, 114703. https://doi.org/10.1016/j.icarus.2021.114703

Kliore. (1974). *Radio occultation exploration of Mars*. D. Reidel Publishing Co.

Kliore, A., Anderson, J., Armstrong, J., Asmar, S., Hamilton, C., Rappaport, N., et al. (2004). Cassini radio science. In *The cassini-huygens mission: Orbiter remote sensing investigations* (pp. 1–70).
Kliore, A. J., Cain, D. L., Fjeldbo, G., Seidel, B. L., Sykes, M. J., & Rasool, S. (1972). The atmosphere of mars from mariner 9 radio occultation measurements. *Icarus*, *17*(2), 484–516. https://doi.org/10.1016/0019-1035(72)90014-0
Langlais, B., Thébault, E., Houliez, A., Purucker, M. E., & Lillis, R. J. (2019). A new model of the crustal magnetic field of mars using mgs and maven. *Journal of Geophysical Research: Planets*, *124*(6), 1542–1569. https://doi.org/10.1029/2018JE005854
Lillis, R. J., Frey, H. V., Manga, M., Mitchell, D. L., Lin, R. P., Acuña, M. H., & Bougher, S. W. (2008). An improved crustal magnetic field map of mars from electron reflectometry: Highland volcano magmatic history and the end of the Martian dynamo. *Icarus*, *194*(2), 575–596. https://doi.org/10.1016/j.icarus.2007.09.032
Lollo, A., Withers, P., Fallows, K., Girazian, Z., Matta, M., & Chamberlin, P. C. (2012). Numerical simulations of the ionosphere of Mars during a solar flare. *Journal of Geophysical Research*, *117*(A5). https://doi.org/10.1029/2011ja017399
Majeed, T., Bougher, S., Withers, P., Haider, S., & Morschhauser, A. (2025). Magnetically controlled ionosphere of mars: A model analysis with the vertical plasma drift effects. *Icarus*, *429*, 116447. https://doi.org/10.1016/j.icarus.2024.116447
Martinis, C. R., Wilson, J. K., & Mendillo, M. J. (2003). Modeling day-to-day ionospheric variability on Mars. *Journal of Geophysical Research*, *108*(A10). https://doi.org/10.1029/2003JA009973
Matta, M., Mendillo, M., Withers, P., & Morgan, D. (2015). Interpreting mars ionospheric anomalies over crustal magnetic field regions using a 2-d ionospheric model. *Journal of Geophysical Research: Space Physics*, *120*(1), 766–777. https://doi.org/10.1002/2014JA020721
Matta, M., Withers, P., & Mendillo, M. (2013). The composition of mars' topside ionosphere: Effects of hydrogen. *Journal of Geophysical Research: Space Physics*, *118*(5), 2681–2693. https://doi.org/10.1002/jgra.50104
Mayyasi, M., & Mendillo, M. (2015). Why the viking descent probes found only one ionospheric layer at Mars. *Geophysical Research Letters*, *42*(18), 7359–7365. https://doi.org/10.1002/2015GL065575
McClintock, W. E., Schneider, N. M., Holsclaw, G. M., Clarke, J. T., Hoskins, A. C., Stewart, I., et al. (2015). The Imaging Ultraviolet Spectrograph (IUVS) for the MAVEN mission. *Space Science Reviews*, *195*(1–4), 75–124. https://doi.org/10.1007/s11214-014-0098-7
Mendillo, M., Marusiak, A. G., Withers, P., Morgan, D., & Gurnett, D. (2013). A new semiempirical model of the peak electron density of the Martian ionosphere. *Geophysical Research Letters*, *40*(20), 5361–5365. https://doi.org/10.1002/2013gl057631
Millour, E., Forget, F., Spiga, A., Pierron, T., Bierjon, A., Montabone, L., et al. (2022). *The Mars climate database (Version 6.1)*. European Planetary Science Congress. Article EPSC2022-786, EPSC2022–786. https://doi.org/10.5194/epsc2022-786
Morgan, D. D., Gurnett, D. A., Kirchner, D. L., Fox, J. L., Nielsen, E., & Plaut, J. J. (2008). Variation of the Martian ionospheric electron density from Mars Express radar soundings. *Journal of Geophysical Research*, *113*(A9). https://doi.org/10.1029/2008ja013313
Němec, F., Morgan, D. D., Gurnett, D. A., Duru, F., & Truhlík, V. (2011). Dayside ionosphere of Mars: Empirical model based on data from the MARSIS instrument. *Journal of Geophysical Research*, *116*(E7), E07003. https://doi.org/10.1029/2010je003789
Nielsen, E., Zou, H., Gurnett, D. A., Kirchner, D. L., Morgan, D. D., Huff, R., et al. (2006). Observations of vertical reflections from the topside Martian ionosphere. *Space Science Reviews*, *126*(1–4), 373–388. https://doi.org/10.1007/s11214-006-9113-y
Oudrhiri, K., Yang, O., Buccino, D., Kahan, D., Withers, P., Tortora, P., et al. (2020). MarCO radio occultation: How the first interplanetary cubesat can help improve future missions. *IEEE Aerospace Conference, 00*, 1–10. https://doi.org/10.1109/aero47225.2020.9172734
Parrott, J. (2024). Esa mars tgo-mex radio occultation v1.0 [Dataset]. *European Space Agency*. https://doi.org/10.57780/ESA-ZDVQ6SW
Parrott, J., Svedhem, H., Witasse, O., Wilson, C., Müller-Wodarg, I., Cardesín-Moinelo, A., et al. (2024). First results of mars express—ExoMars trace gas orbiter mutual radio occultation. *Radio Science*, *59*(7). https://doi.org/10.1029/2023rs007873
Pätzold, M., Neubauer, F. M., Carone, L., Hagermann, A., Stanzel, C., Häusler, B., et al. (2004). MaRS: Mars express orbiter radio science. In *Mars express: The scientific payload ADS bibcode* (Vol. 1240, pp. 141–163). 2004ESASP1240..141P. Retrieved from https://ui.adsabs.harvard.edu/abs/2004ESASP1240..141P
Peter, K., Pätzold, M., Montabone, L., Thiemann, E., González-Galindo, F., Witasse, O., et al. (2023). The effects of atmospheric dust and solar radiation on the dayside ionosphere of Mars derived from 17 years of Mars Express radio science observations. *Icarus*, *400*, 115565. Article 115565, 115565. https://doi.org/10.1016/j.icarus.2023.115565
Pilinski, M., Andersson, L., Fowler, C., Peterson, W. K., Thiemann, E., & Elrod, M. K. (2019). Electron temperature response to solar forcing in the low-latitude Martian ionosphere. *Journal of Geophysical Research: Planets*, *124*(11), 3082–3094. https://doi.org/10.1029/2019JE006090
Safaeinili, A., Kofman, W., Mouginot, J., Gim, Y., Herique, A., Ivanov, A. B., et al. (2007). Estimation of the total electron content of the Martian ionosphere using radar sounder surface echoes. *Geophysical Research Letters*, *34*(23). https://doi.org/10.1029/2007gl032154
Sánchez-Cano, B., Lester, M., Witasse, O., Milan, S. E., Hall, B. E. S., Cartacci, M., et al. (2016). Solar cycle variations in the ionosphere of Mars as seen by multiple Mars Express data sets. *Journal of Geophysical Research: Space Physics*, *121*(3), 2547–2568. https://doi.org/10.1002/2015ja022281
Sánchez-Cano, B., Radicella, S., Herraiz, M., Witasse, O., & Rodríguez-Caderot, G. (2013). NeMars: An empirical model of the Martian dayside ionosphere based on Mars Express MARSIS data. *Icarus*, *225*(1), 236–247. https://doi.org/10.1016/j.icarus.2013.03.021
Schunk, R., & Nagy, A. (2009). *Ionospheres: Physics, plasma physics, and chemistry* (2nd ed.). Cambridge University Press.
Segale, J., Felici, M., Withers, P., & Curry, S. (2024). Characterization of the m1 and m2 layers in the undisturbed Martian ionosphere at a variety of solar conditions with maven rose. *Icarus*, *424*, 116251. https://doi.org/10.1016/j.icarus.2024.116251
Tian, R., Jiang, C., Yang, G., Yin, W., Zhang, Y., & Zhao, Z. (2022). Solar cycle and seasonal variability of Martian ionospheric irregularities from Mars atmosphere and volatile evolution observations. *The Astrophysical Journal*, *931*(1), 18. https://doi.org/10.3847/1538-4357/ac61d5
Vogt, M. F., Withers, P., Fallows, K., Flynn, C. L., Andrews, D. J., Duru, F., & Morgan, D. D. (2016). Electron densities in the ionosphere of Mars: A comparison of MARSIS and radio occultation measurements. *Journal of Geophysical Research: Space Physics*, *121*(10), 10241–10257. https://doi.org/10.1002/2016ja022987
Withers, P. (2009). A review of observed variability in the dayside ionosphere of Mars. *Advances in Space Research*, *44*(3), 277–307. https://doi.org/10.1016/j.asr.2009.04.027
Withers, P. (2020). Revised predictions of uncertainties in atmospheric properties measured by radio occultation experiments. *Advances in Space Research*, *66*(10), 2466–2475. https://doi.org/10.1016/j.asr.2020.07.049
Withers, P., Felici, M., Hensley, K., Mendillo, M., Barbinis, E., Kahan, D., et al. (2023). The ionosphere of mars from solar minimum to solar maximum: Dayside electron densities from maven and mars global surveyor radio occultations [The Mars upper atmosphere at solar minimum]. *Icarus*, *393*, 114508. https://doi.org/10.1016/j.icarus.2021.114508
Withers, P., Felici, M., Mendillo, M., Moore, L., Narvaez, C., Vogt, M. F., et al. (2020). The MAVEN radio occultation science experiment (ROSE). *Space Science Reviews*, *216*(4), 61. Article 61. https://doi.org/10.1007/s11214-020-00687-6

Withers, P., Felici, M., Mendillo, M., Vogt, M. F., Barbinis, E., Kahan, D., et al. (2022). Observations of high densities at low altitudes in the nightside ionosphere of mars by the maven radio occultation science experiment (rose). *Journal of Geophysical Research: Space Physics*, *127*(11), e2022JA030737. https://doi.org/10.1029/2022JA030737

Withers, P., Felici, M., Segale, J., Barbinis, E., Kahan, D., & Oudrhiri, K. (2024). Several outstanding issues concerning the ionosphere of Mars. *Earth Planets and Space*, *76*(1), 95. https://doi.org/10.1186/s40623-024-02036-1

Withers, P., Weiner, S., & Ferreri, N. R. (2015). Recovery and validation of Mars ionospheric electron density profiles from Mariner 9. *Earth Planets and Space*, *67*(1), 194. https://doi.org/10.1186/s40623-015-0364-2

Zhang, M. H. G., Luhmann, J. G., & Kliore, A. J. (1990). An observational study of the nightside ionospheres of Mars and Venus with radio occultation methods. *Journal of Geophysical Research*, *95*(A10), 17095–17102. https://doi.org/10.1029/ja095ia10p17095